MDPI

Article

Penetration and Displacement Behavior of N_2 in Porous Interlayer Structures Containing Water/Salt Component by Molecular Dynamics Simulation

Zhibin Jiang [1,2,*], Liqiang Sima [1], Lisha Qi [2], Xiaoguang Wang [2], Jie Wang [2], Zhenpeng Leng [3,4] and Tianpeng Zhao [4]

[1] School of Geoscience and Technology, Southwest Petroleum University, Chengdu 610500, China; donghao15610029171@163.com
[2] Research Institute of Exploration and Development, PetroChina Xinjiang Oilfield Company, Karamay 834000, China; 15856956521@163.com (L.Q.); mengchen0628@163.com (X.W.); 17860739118@163.com (J.W.)
[3] Institute of Mechanics, Chinese Academy of Sciences, Beijing 100190, China; lengsnupc@163.com
[4] Oleum Technologies (Beijing) Company Limited, Beijing 102206, China; xhl15621429029@163.com
[*] Correspondence: zhaizhai20212021@163.com

Academic Editor: Riccardo Chelli

Abstract: The penetration and displacement behavior of N_2 molecules in porous interlayer structures containing a water/salt component with porosities of 4.29%, 4.73%, 5.17%, 7.22%, and 11.38% were explored using molecular dynamics simulations. The results demonstrated that the large porosity of the interlayer structures effectively enhanced the permeation and diffusion characteristics of N_2. The water and salt in the interlayer structures were displaced during the injection of N_2 in the porosity sequence of 4.29% < 4.73% < 5.17% < 7.22% < 11.38%. The high permeance of 7.12×10^{-6} indicated that the interlayer structures with a porosity of 11.38% have better movability. The strong interaction of approximately 15 kcal/mol between N_2 and H_2O had a positive effect on the diffusion of N_2 and the displacement of H_2O before it reached a stable equilibrium state. The distribution of N_2 in porous interlayer structures and the relationship between the logarithm of permeability and breakthrough pressure were presented. This work highlighted the effects of porosity on the permeability and diffusion of N_2/H_2O in the interlayer, thus providing theoretical guidance for the development of petroleum resources.

Keywords: molecular dynamics simulation; penetration and displacement; porous interlayer structures

1. Introduction

Oil has aroused growing attention as a crucial energy resource around the world [1–3]. Oilfield exploration technology is vigorously investigated to discover more oil resources [4–6]. The porous interlayer is one of the most important factors affecting the distribution of the remaining oil, which increases the heterogeneity of the reservoir [7], complicates the oil–water movement relationship [8], and disorders the distribution regularity of the remaining oil [9,10]. Previous studies have mainly focused on explaining the influence of the interlayer on oil–gas movement [11]. By exploring the effect of three types of interlayers on oil–water movement and the formation of rised water, Wang et al. [12] found that the oil layer can be divided into several connected or disconnected units and that it controls the movement of oil and water and ultimately affects the distribution of remaining oil. Luo et al. [13] discovered that the vertical migration interval of the oil and gas in the heterogeneous transport layer is hindered by the interlayer, thus complicating the migration path. Wu et al. [14] found that the interlayer restricts the vertical permeability of the reservoir. These results indicated that the interlayer has an important influence on oilfield exploration technology [15]. Considering the complexity of experimental conditions, theoretical calculation provides an effective way to explore the interlayer. The process of

gases, including CO_2 and N_2, passing through the interlayer is the best method to define structural features. Fang et al. found that slug injection of CO_2 was a promising technology for the enhancement of oil recovery in an MD simulation. However, few studies have focused on the injection of N_2 into the interlayer [3], which could effectively open the channel for the migration of oil and gas and cause the remaining water/salt component to be the only substances in the interlayer. Therefore, it is vital to elucidate the effects of porosity on the interlayer for N_2 penetration, H_2O displacement behavior, and the diffusion mechanism.

In this work, we investigated the penetration and displacement behavior of N_2 in interlayers containing a water/salt component and with porosities of 4.29%, 4.73%, 5.17%, 7.22%, and 11.38% using molecular dynamics (MD) simulations. First, porous SiO_2 was built to simulate the interlayers. Subsequently, the pores of SiO_2 were filled with a salt solution, followed by the displacement of N_2 molecules under breakthrough pressure. Next, the diffusion process and mean squared displacement were calculated in consideration of the porosity and pressure effects. Then, the gas distribution and the permeability–pressure relationship were analyzed to show the microscopic mechanism of N_2/water/salt passing through the interlayer. Our results highlight the potential impact of the interlayer on the gas diffusion process, providing theoretical guidance for oil exploitation.

2. Model and Method

The silica structure was selected as a typical mineral component [16]. The generation of the frameworks was conducted using a $10 \times 10 \times 10$ supercell of silica structure with dimensions (xyz) of 71.60 Å $\times$ 71.60 Å $\times$ 71.60 Å. Considering that the remaining oil exists in interlayer structures with porosities of 4–8% [17], pores along the *z*-axis with porosities of 4.29%, 4.73%, 5.27%, 7.22%, and 11.38% were established in the center of the silica structures. These structures were tagged as P4.29%, P4.73%, P5.27%, P7.22%, and P11.38%. Furthermore, the silica structures used in this study were rigid and fixed, and the silica surface of the pore was hydroxylated and set at 9.6 nm^{-2} [17].

MD regards all matter as a particle system composed of atoms and molecules, and the motion of all particles complies with the laws of classical mechanics or quantum mechanics. The most important characteristic of MD is that it ignores the interactions of atoms between electrons and electrons and the electrons and the nucleus, only regarding the atom as a basic unit to calculate the energy of the whole system and thus greatly improving the computational efficiency, making the MD method applicable to larger computing systems. Therefore, the MD simulation was adopted to complete these calculations. A saline solution with an H_2O to salt molar ratio of 1000:1 [18] was uniformly distributed in the hydroxylated silica pores to simulate the formation of brine. An N_2 molecule box was placed on the left side of the silica structures in order to create a pressure differential in the initial model. A vacuum slab was placed on the right side of the silica structures. A rigid graphene sheet was placed on the left side of the N_2 flooding and the right side of the vacuum slab as a rigid piston (Figure 1). For the system, the pores were uniformly filled with water/salt at the initial moment. A 1 ns equilibrium MD simulation with the NVT ensemble was conducted to achieve an equilibrium state [19].
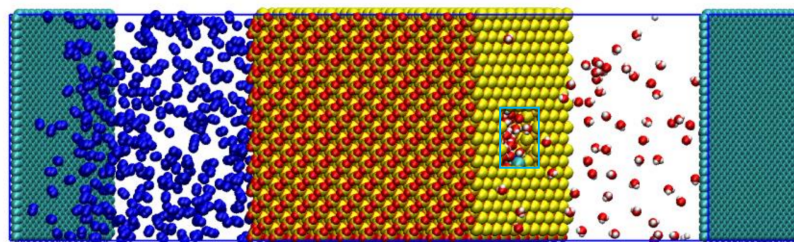

Figure 1. Initial configurations of N_2 in the porous interlayer.

The well-known 12–6 Lennard–Jones potential $4\varepsilon[(\sigma/r)^{12} - (\sigma/r)^6]$ [20] was used to calculate the van der Waals interaction, where r represents the distance between two atoms. The cutoff distance was set to 11 Å. The rigid SPC/E model [21] was used for modeling water molecules with the SHAKE algorithm [22], while the Lennard–Jones potential was adopted to model the neutral N_2 [23]. The silica surface was modeled by the CLAYFF [24] force field. All MD simulations were performed in the NVT ensemble (the number of molecules, volume, and temperature were constant) with a time step of 1 fs [25]. The temperature, kept at 298 K, was controlled by a Nosé–Hoover thermostat [26], and every 1000 steps, a frame was set for data analysis. LAMMPS software [27] was employed, and total simulation was conducted for 1 ns. The application of the periodic boundary condition was done in all directions [28]. The desired transmembrane pressure in the experiments was applied to the feed piston to push the water/salt across the membrane.

3. Discussion

During the injection process, N_2 passed through the pores of SiO_2 with breakthrough pressures of 35.83, 14.00, 11.18, 5.77, and 0.50 MPa, which were selected to put the interlayer porosities of 4.29%, 4.73%, 5.17%, 7.22%, and 11.38% in the displacement systems, according to the experimental data (offered by the Research Institute of Exploration and Development, PetroChina Xinjiang Oilfield Company). Breakthrough pressures were applied to the rigid graphene sheet.

3.1. Displacement of Water/Salt by N_2

Figure 2 presents the process snapshots of N_2 injection in the porosities of 4.29%, 4.73%, 5.17%, 7.22%, and 11.38%. For a certain porosity, H_2O, Na^+, and Cl^- ions were displaced after the injection of N_2, and the displacement degree of H_2O, Na^+, and Cl^- gradually increased with time. Taking the structure with a porosity of 4.29% as an example, all N_2 molecules were gathered on the left side of the SiO_2 initially. After 0.3 ns, some N_2 molecules passed through the SiO_2 phase, and meanwhile, some H_2O, Na^+, and Cl^- were displaced into the vacuum phase and the N_2 phase. With an increase in simulation time, more N_2, H_2O, Na^+, and Cl^- passed through the SiO_2 phase until the system reached equilibrium at 0.7 ns. In comparison, the larger porosities led to more evident displacement phenomena after a period of time. When the porosity was 11.38%, almost all the H_2O dissolved into the N_2 phase. Detailed observations indicated that after injecting N_2, all components were in dynamic equilibrium within the interlayer after 1 ns.
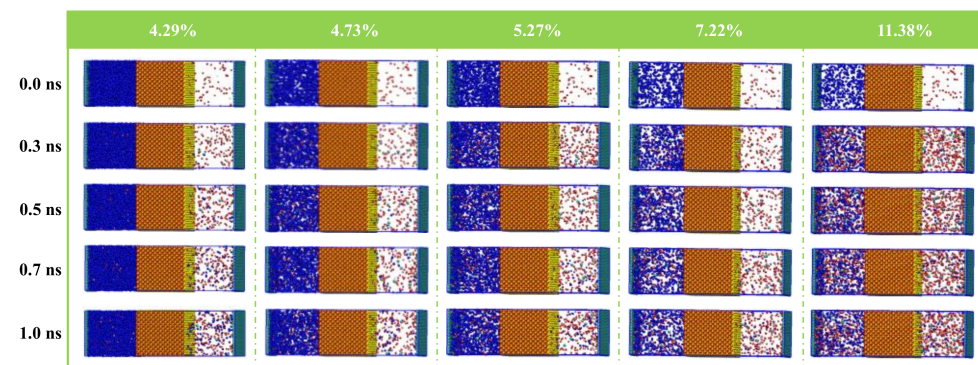

Figure 2. Side views for the evolution of N_2 flooding from 0 to 1 ns.

To analyze the displacement process, the center of mass (COM) of N_2 was explored, as shown in Figure 3. For certain interlayer structures, the COM of N_2 moved toward the right of the interlayer structures. After 0.3 ns, the COM of N_2 moved -0.65 Å, -2.52 Å, -1.30 Å, -2.24 Å, and -1.93 Å for P4.29%, P4.73%, P5.27%, P7.22%, and P11.38%, respectively. In other words, the COM of N_2 moved far toward the left of the interlayer structures at the beginning of the simulation, except for the structure with a porosity of 4.29%. This was

attributed to the achievement of an equilibrium state. In the next 0.7 ns, the COM of N_2 moved toward the right of the interlayer structures with moving distances of 5.66 Å, 5.87 Å, 7.74 Å, 7.14 Å, and 16.29 Å for P4.29%, P4.73%, P5.27%, P7.22%, and P11.38%, respectively. After the same simulation time, large porosity led to an increase in the movement distance of the COM, which was consistent with the process snapshot analysis. For P11.38%, the large pore size led to more gas molecules passing through interlayer structures, resulting in a faster passing process than other structures. Therefore, the curve of P11.38% shows an extremum and a large slope.
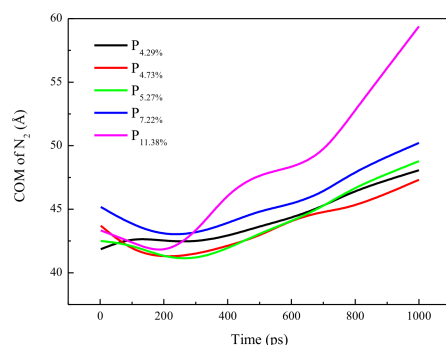

Figure 3. The location of the center of mass of N_2.

3.2. Movability Evaluation

Permeance is an indispensable indicator to determine the displacement efficiency of N_2 over water/salt [3]. Table 1 shows the permeances of N_2 passing through SiO_2 with five interlayer structures with different porosities. As the porosity increased, the permeance of N_2 gradually increased in the sequence of P4.29% < P4.73% < P5.27% < P7.22% < P11.38%. A large pore size results in a small barrier, resulting in a small N_2 energy repulsion. Moreover, the weak interaction guarantees that the gas molecules pass through the pores of SiO_2 rapidly.

Table 1. The permeances of N_2 passing through the five interlayers.

Porosity	4.29%	4.73%	5.27%	7.22%	11.38%
Permeability	1.57×10^{-6}	1.83×10^{-6}	2.39×10^{-6}	3.09×10^{-6}	7.12×10^{-6}

In order to evaluate the diffusion behavior and movability of N_2 and H_2O molecules, mean squared displacement (MSD) [29,30] was calculated:

$$MSD = |R_i(t) - R_i(0)|^2 \tag{1}$$

where $R_i(t)$ represents the position of i atom at t time, and $R_i(0)$ represents the initial position. Each pore was divided into eleven layered blocks, and MSD was calculated for each structure. Previous studies confirmed that the gas diffusion rate was positively correlated with the slope of the MSD profile. As exhibited in Figure 4a, on the whole, the MSD of H_2O along the *z*-axis in the five interlayers increased sharply at the beginning of the simulation (0–200 ps). The slope of the MSD followed the sequence of P11.38% > P7.22% > P5.27% > P4.73% > P4.29%. In particular, the structure with a porosity of 11.38% showed the fastest gas diffusion because the large pore size enhanced the H_2O diffusion rate. After the initial increase in the MSD, the slope of the MSD flattened out to a constant value because of the equilibrium state of the system. During this period (200–1000 ps), the equilibrated MSD of H_2O followed the sequence of P11.38% > P7.22% > P5.27% > P4.73% > P4.29%. The trend of the MSD curve agreed well with the physical characteristics and porosity of the pores.
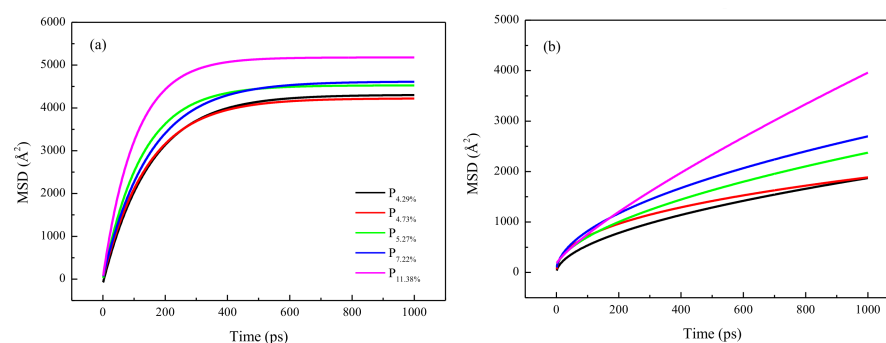
Figure 4. The mean squared displacement of H_2O (**a**) and N_2 (**b**).

Figure 4b delineates the MSD of N_2 along the *z*-axis in the nanopores of SiO_2 with an increase in time. Larger porosity significantly boosted the diffusion capacity of N_2. During the simulation, the porosity of the interlayer structures increased from P4.29% to P4.73%, P5.27%, P7.22%, and P11.38%, and the equilibrated MSD of N_2 increased to 0.17%, 33.44%, 45.11%, and 117.61%. This result confirms that the MSD of N_2 is more significantly enhanced by the large porosity of P11.38% than by those of other structures. Conversely, the MSD of H_2O is more affected by porosity. In short, increasing porosity can enhance the MSD of H_2O more than that of N_2 at both early and late stages of the simulation, particularly for the large P11.38%. Therefore, it can be envisioned that large porosity can greatly promote the diffusion of N_2 in SiO_2 for the displacement of water and salt. Higher mobility of the gas molecules in the middle of the interlayer was observed for structures with large porosity, and the moving ability near the small silica surface was poor. However, over time, the overall effect of the H_2O slug flooding became more severe than that of N_2.

3.3. Distribution of H_2O, N_2, and Salt in Interlayer Structure

In order to evaluate the distribution of the H_2O, N_2, and salt in the Z direction visually, the relative concentration profiles over 1 ns were calculated, as shown in Figure 5. On the *z*-axis, the range of 0–71 Å represents the N_2 phase, the range of 75–165 Å represents the porous SiO_2 phase, and the range of 170–240 Å is the vacuum phase. The rigid graphene sheet was placed on the left side of the N_2 flooding and the right side of the vacuum slab as a rigid piston. Initially, most of the H_2O, Na^+, and Cl^- was in the pores of the SiO_2. After 100 ps, the density difference of the N_2/H_2O/salt at the SiO_2 interface gradually diminished, while a substantial change in the density of the N_2/H_2O/salt inside and outside the pores of the SiO_2 took place. The small pore size of the SiO_2 with a porosity of 4.29% limited the number of molecules in the free phase, resulting in almost no N_2 molecules left in the pores. The lower porosity led to a smaller volume to fill. And less N_2 in the free phase. However, some H_2O with dipole moment, Na^+, and Cl^- ions existed in the pores of the SiO_2, which is explained by the larger porosity. On the whole, some N_2 molecules can pass through the pores of the SiO_2 into the vacuum phase in all five systems under the breakthrough pressure. However, most N_2 molecules remain in the pristine N_2 phase. The high peak in the range of 0–10 Å was attributed to N_2 adsorption in the graphene sheet surface, and another peak in the range of 75–80 Å was attributed to N_2 adsorption in the SiO_2 surface, while the remaining N_2 molecules were uniformly distributed. The H_2O and salt diffused from the pores of the SiO_2 into the N_2 and vacuum phase, and the number of H_2O, Na^+, and Cl^- ions in the N_2 phase was smaller than that in the vacuum phase. The results show that N_2 slugs can effectively displace the saline solution in the pores of the SiO_2 into the vacuum phase.
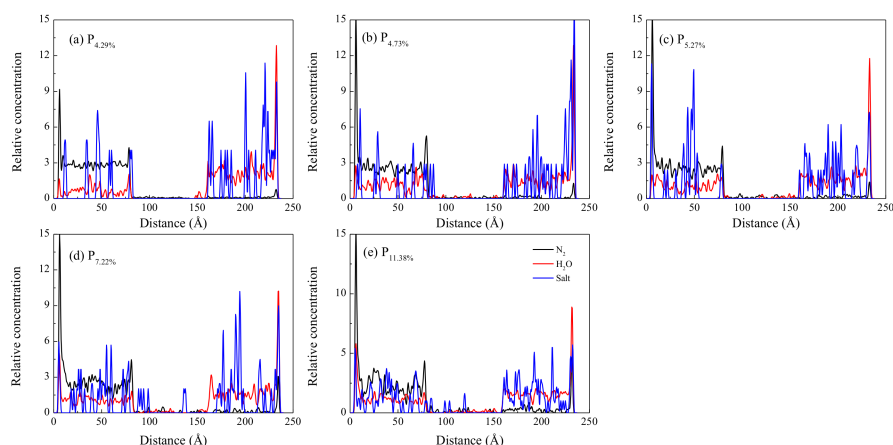
Figure 5. Relative concentration distribution of N_2, H_2O, and Salt along z-axis.

3.4. Interaction between N_2 and H_2O

Figure 6 presents the interaction energy between N_2 and H_2O with simulation time. The interaction between N_2 and H_2O was negative during the whole process, and large negative values indicate a strong interaction between N_2 and H_2O. Overall, as the time increased, the interaction energy between N_2 and H_2O initially increased rapidly and then plateaued to a constant. From 0 ps to 200 ps, the interaction energy increased from 0 to -31.48, -26.89, -24.56, -23.85, and -16.54 kcal/mol for P4.29%, P4.73%, P5.27%, P7.22%, and P11.38%, respectively. The interaction energy followed the sequence P11.38% < P7.22% < P5.27% < P4.73% < P4.29%, which agreed with the porosity of SiO_2. This result implies that few N_2 and H_2O molecules are initially in contact with each other at the interface between N_2 slugs and SiO_2, and more N_2 molecules were in contact with H_2O as time increased until the system reaches equilibrium. The interaction in P4.29% was much higher than that in other structures because of the strengthened interaction between N_2 and H_2O by the small pore size. During the simulation time of 200–1000 ps, N_2 molecules passed through the pores of the SiO_2, and H_2O molecules diffused into the N_2 box as well as the vacuum phase.
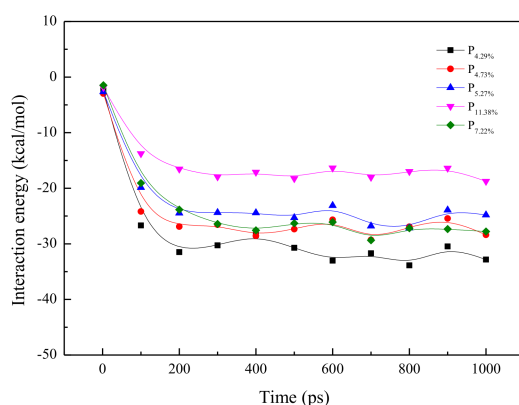

Figure 6. The interaction relationship between N_2 and H_2O with the increase in time.

3.5. The Relationship between the Parameters

To investigate the relationship between permeability, porosity, and breakthrough pressure, the proper function fittings are discussed. Figure 7a shows the relationship between the permeability of N_2 and the breakthrough pressure of N_2. After logarithm fetching on the permeability of N_2 (Log(K)), a linear relationship with the logarithm fetch breakthrough pressure of N_2 (Log(P)) was given. The fitting formula is Log(P) = $-0.775 \times$ Log(K) $- 3.298$, which is in agreement with the experimental results of Log(P) = $-0.658 \times$

Log(K) − 0.557, which was called by log–log analysis. The same order of magnitude for the line slope and the experimental results shows the rationality of the model and accuracy of the calculation parameters. Furthermore, the large permeability can be obtained by adjusting the breakthrough pressure according to the fitting formula. In addition, the intersection profile of the porosity and gas injection breakout pressure was fitted, indicating an exponential relationship between them. The large porosity corresponds to smaller breakout pressure according to the fitting formula. In order to show the relationship between porosity (P) and permeability (p), their fitting profile is shown in Figure 7b. The fitting formula is $P = 1.13 \times 10^7 \times e^{-8.71\,p}$, which is a typical exponential relationship. In the process of oil and gas exploitation, the character of the pore structure is first acquired, the gas injection breakout pressure is calculated next by the intersection profile, and last, the permeability is predicted by log–log analysis in theoretical calculations.
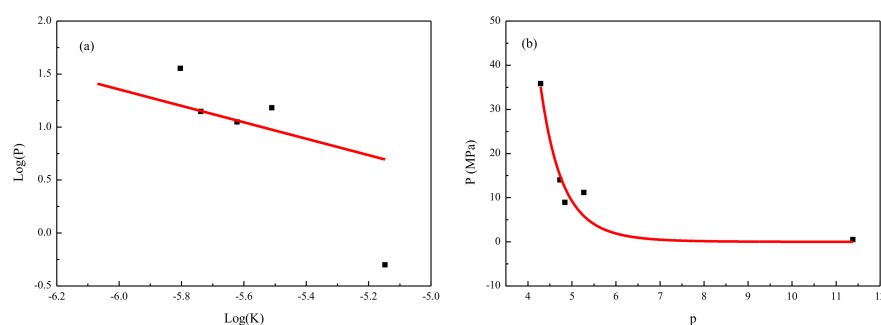

Figure 7. (**a**) The relationship between permeability and breakthrough pressure; (**b**) the relationship between permeability and porosity.

4. Conclusions

The penetration and displacement behavior of molecules in interlayers with different porosities were analyzed using molecular dynamics simulations. The results show that interlayers with different pore sizes and porosities can strongly affect the distribution, diffusion, and displacement processes. The MSD and gas distribution show that N_2 can pass through the pores of interlayer structures and displace the H_2O, Na^+, and Cl^- in the pore space into the vacuum phase. This shows that high porosity can result in high-efficiency diffusion of N_2, and high porosity in porous interlayers benefit the displacement of H_2O, Na^+, and Cl^-. Interaction analysis between N_2 and H_2O confirms that a strong interaction between N_2 and water can overcome the interaction between water and the pore wall to render rapid displacement of H_2O, Na^+, and Cl^-. A log–log analysis and an intersection profile were presented to theoretically predict the relationship between permeability, porosity, and breakthrough pressure.

Institutional Review Board Statement: Not applicable.

Informed Consent Statement: Not applicable.

Data Availability Statement: No new data were created or analyzed in this study. Data sharing is not applicable to this article.

Conflicts of Interest: The authors declare no conflict of interest.

References

1. Zhe, C.; Haijun, J.; Yang, L.; Ruyue, W.; Zhaojie, X. Progress and development directions of deep oil and gas exploration and development in China. *China Petrol. Explor.* **2020**, *25*, 45–57.
2. Kumar, R.; Strezov, V.; Weldekidan, H.; He, J.; Singh, S.; Kan, T.; Dastjerdi, B. Lignocellulose biomass pyrolysis for bio-oil production: A review of biomass pre-treatment methods for production of drop-in fuels. *Renew. Sust. Energ. Rev.* **2020**, *123*, 109763. [CrossRef]
3. Zhou, S.; Wang, Z.; Wang, M.; Wang, J.; Wei, S.; Guo, W.; Lu, X. Nanoporous boron nitride membranes for helium separation. *ACS Appl. Nano Mater.* **2019**, *2*, 4471–4479. [CrossRef]
4. Li, S.; Lu, C.; Wu, M.; Hu, Z.; Li, Z.; Wang, Z. New insight into CO_2 huff-n-puff process for extraheavy oil recovery via viscosity reducer agents: An experimental study. *J. CO_2 Util.* **2020**, *42*, 101312. [CrossRef]
5. Yuan, S.; Wang, Q. New progress and prospect of oilfields development technologies in China. *Petrol. Explor. Dev.* **2018**, *45*, 698–711. [CrossRef]
6. Zhou, S.; Wang, M.; Wang, J.; Xin, H.; Liu, S.; Wang, Z.; Wei, S.; Lu, X. Carbon phosphides: Promising electric field controllable nanoporous materials for CO_2 capture and separation. *J. Mater. Chem. A* **2020**, *8*, 9970–9980. [CrossRef]
7. Al-Khdheeawi, E.A.; Vialle, S.; Barifcani, A.; Sarmadivaleh, M.; Iglauer, S. Effect of wettability heterogeneity and reservoir temperature on CO_2 storage efficiency in deep saline aquifers. *Int. J. Greenh. Gas Control.* **2018**, *68*, 216–229. [CrossRef]
8. Liu, W.; Tan, C.; Dong, X.; Dong, F.; Murai, Y. Dispersed oil–water two-phase flow measurement based on pulse-wave ultrasonic doppler coupled with electrical sensors. *IEEE T. Instrum. Meas.* **2018**, *67*, 2129–2142. [CrossRef]
9. Shijun, H.; Hao, X.; Shaolei, W.; Chenghui, H.; Yang, Y. Physical simulation of the interlayer effect on SAGD production in mackay river oil sands. *Fuel* **2016**, *183*, 373–385. [CrossRef]
10. Shi, X.; Wang, P.; Wang, L.; Bai, Y.; Xie, H.; Zhou, Y.; Wang, J.A.; Li, Z.; Qu, L.; Shi, M.; et al. Few layered BiOBr with expanded interlayer spacing and oxygen vacancies for efficient decomposition of real oil field produced wastewater. *ACS Sustain. Chem. Eng.* **2018**, *6*, 13739–13746. [CrossRef]
11. Ho, T.A.; Wang, Y.; Jové Colón, C.F.; Coker, E.N. Fast advective water flow through nanochannels in clay interlayers: Implications for moisture transport in soils and unconventional oil/gas production. *ACS Appl. Nano Mater.* **2020**, *3*, 11897–11905. [CrossRef]
12. Wang, C.; Yang, H.; Le, P.J.B.; Su, B. Rigin of interbeds and the influence on distribution of remaining oil—taking command of the hudson donghe sandstone oilfiled. *Xinjiang Oil Gas* **2019**, *15*, 15–20.
13. Luo, X.R.; Zhang, L.Q.; Zhang, L.K.; Lei, Y.H.; Cheng, M.; Shi, H.; Cao, B.F. Heterogeneity of clastic carrier bed and hydrocarbon migration and accumulation. *Acta Pet. Sin.* **2020**, *41*, 253–272.
14. Yuetian, W.J.L. Influence Across the Mezzanine Level on the Development Effect of Fracturing for Horizontal Well. *Well Test.* **2011**, *20*, 37–39.
15. Zhou, S.; Wang, M.; Wei, S.; Cao, S.; Wang, Z.; Liu, S.; Sun, D.; Lu, X. First-row transition-metal-doped graphyne for ultrahigh-performance CO_2 capture and separation over $N_2/CH_4/H_2$. *Mater. Today Phys.* **2021**, *16*, 100301. [CrossRef]
16. Hosseini, S.S.; Teoh, M.M.; Chung, T.S. Hydrogen separation and purification in membranes of miscible polymer blends with interpenetration networks. *Polymer* **2008**, *49*, 1594–1603. [CrossRef]
17. Fang, T.; Wang, M.; Gao, Y.; Zhang, Y.; Yan, Y.; Zhang, J. Enhanced oil recovery with CO_2/N_2 slug in low permeability reservoir: Molecular dynamics simulation. *Chem. Eng. Sci.* **2019**, *197*, 204–211. [CrossRef]
18. Lyu, Q.; Sun, S.; Li, C.; Hu, S.; Lin, L.C. Rational Design of two-dimensional hydrocarbon polymer as ultrathin-film nanoporous membranes for water desalination. *ACS Appl. Mater. Interfaces* **2018**, *10*, 18778–18786. [CrossRef]
19. Zhou, S.; Lu, X.; Wu, Z.; Jin, D.; Guo, C.; Wang, M.; Wei, S. Diffusion and separation of CH_4/N_2 in pillared graphene nanomaterials: A molecular dynamics investigation. *Chem. Phys. Lett.* **2016**, *660*, 272–276. [CrossRef]
20. Heinz, H.; Vaia, R.A.; Farmer, B.L.; Naik, R.R. Accurate simulation of surfaces and interfaces of face-centered cubic metals using 12−6 and 9−6 lennard-jones potentials. *J. Phys. Chem. C* **2008**, *112*, 17281–17290. [CrossRef]
21. Berendsen, H.J.C.; Grigera, J.R.; Straatsma, T.P. The missing term in effective pair potentials. *J. Phys. Chem.* **1987**, *91*, 6269–6271. [CrossRef]
22. Ryckaert, J.-P.; Ciccotti, G.; Berendsen, H.J.C. Numerical integration of the cartesian equations of motion of a system with constraints: Molecular dynamics of n-alkanes. *J. Comput. Phys.* **1977**, *23*, 327–341. [CrossRef]
23. Chae, K.; Violi, A. Mutual diffusion coefficients of heptane isomers in nitrogen: A molecular dynamics study. *J. Chem. Phys.* **2011**, *134*, 044537. [CrossRef] [PubMed]
24. Cygan, R.T.; Liang, J.J.; Kalinichev, A.G. Molecular models of hydroxide, oxyhydroxide, and clay phases and the development of a general force field. *J. Phys. Chem. B* **2004**, *108*, 1255–1266. [CrossRef]
25. Hoover, W.G. Canonical dynamics: Equilibrium phase-space distributions. *Phys. Rev. A* **1985**, *31*, 1695–1697. [CrossRef]
26. Nosé, S. A molecular dynamics method for simulations in the canonical ensemble. *Mol. Phys.* **1984**, *52*, 255–268. [CrossRef]
27. Plimpton, S. Fast parallel algorithms for short-range molecular dynamics. *J. Comput. Phys.* **1995**, *117*, 1–19. [CrossRef]
28. Nguyen, V.D.; Béchet, E.; Geuzaine, C.; Noels, L. Imposing periodic boundary condition on arbitrary meshes by polynomial interpolation. *Comput. Mater. Sci.* **2012**, *55*, 390–406. [CrossRef]

29. Xu, Z.; Yuan, S.L.; Yan, H.; Liu, C.B. Adsorption of histidine and histidine-containing peptides on Au(111): A molecular dynamics study. *Colloid. Surfaces A* **2011**, *380*, 135–142. [CrossRef]
30. Gholizadeh, R.; Wang, Y. Molecular dynamics simulation of the aggregation phenomenon in the late stages of silica materials preparation. *Chem. Eng. Sci.* **2018**, *184*, 62–71. [CrossRef]